Quantifying calcium fluxes underlying calcium puffs in *Xenopus laevis* oocytes

Luciana Bruno[*,§,†], **Guillermo Solovey**[*,†], **Alejandra C. Ventura**[*], **Sheila Dargan**[#], and **Silvina Ponce Dawson**[*,§]

[*] Departamento de Física, Facultad de Ciencias Exactas y Naturales, UBA, Ciudad Universitaria, Pabellón I, (1428) Buenos Aires, Argentina.

[#] Departments of Neurobiology & Behavior and Physiology & Biophysics, University of California Irvine, CA 92697-4550, USA.

[§] CONICET, Argentina

Summary

We determine the calcium fluxes through inositol 1,4,5-trisphosphate receptor/channels underlying calcium puffs of *Xenopus laevis* oocytes using a simplified version of the algorithm of Ventura et al., 2005 [1]. An analysis of 130 puffs obtained with Fluo-4 indicates that Ca^{2+} release comes from a region of width ~ 450 nm, that the release duration is peaked around 18ms and that the underlying Ca^{2+} currents range between 0.12 and 0.95pA. All these parameters are independent of IP_3 concentration. We explore what distributions of channels that open during a puff, N_p, and what relations between current and number of open channels, $I(N_p)$, are compatible with our findings and with the distribution of puff-to-trigger amplitude ratio reported in Rose et al, 2006 [2]. To this end, we use simple "mean field" models in which all channels open and close simultaneously. We find that the variability among clusters plays an important role in shaping the observed puff amplitude distribution and that a model for which $I(N_p) \sim N_p$ for small N_p and $I(N_p) \sim N_p^{1/\alpha}$ ($\alpha > 1$) for large N_p, provides the best agreement. Simulations of more detailed models in which channels open and close stochastically show that this nonlinear behavior can be attributed to the limited time resolution of the observations and to the averaging procedure that is implicit in the mean-field models. These conclusions are also compatible with observations of ~400 puffs obtained using the dye Oregon green.

1. Introduction

The term "puff" refers to a localized increase in fluorescence that arises as a consequence of the liberation of calcium ions from the endoplasmic reticulum into the cytosol through inositol (1,4,5)-trisphosphate receptor channels (IP_3R's). Puffs have been observed, in particular, in *Xenopus laevis* oocytes where the channels are preferentially located within a 6μm thick band a few micrometers away from the cell surface [3] and are thought to be condensed in clusters.

Distances between channels within a cluster are thought to be of a few hundred nanometers [2,4,5], while inter-cluster distances are of a few micrometers.

Due to their internal localization in the cell, the Ca^{2+} current passing through these channels under physiological conditions cannot be measured by electrophysiological techniques. Instead, optical techniques provide an alternative approach to address this issue. Sun et al. [6] obtained estimates of the calcium flux associated with individual events in *Xenopus laevis* oocytes by integrating fluorescence profiles along a linescan in three dimensions to derive the signal mass as a function of time. Rates of signal mass rise corresponded to Ca^{2+} currents of 0.4 - 2.5 pA, though there was considerable variability in magnitudes and durations of Ca^{2+} flux between successive puffs and between different puff sites. Thul and Falcke [7] simulated the current and concentration profiles generated by Ca^{2+} release from the endoplasmic reticulum and compared these results with signal mass measurements in *Xenopus laevis* oocytes. They found that the release current was approximately proportional to the square root of the number of open channels in a cluster and depended linearly on the concentration of free Ca^{2+} in the lumen. The magnitudes of the Ca^{2+} currents estimated in that paper ranged from 0.015 pA (low Ca^{2+} concentration in the lumen, one open channel) to 0.8 pA (high Ca^{2+} concentration in the lumen, 36 open channels).

"Trigger" events, small Ca^{2+} signals that immediately precede puffs [2], were used in [4] to estimate the properties of Ca^{2+} fluxes during puffs observed in *Xenopus laevis* oocytes. To this end, a "forward method" was applied to generate numerically simulated images that were then compared to the experimental ones. The number (~25-35), single channel current (~0.4pA) and spatial distribution of the IP_3R's (uniformly distributed over a region of size ~300-800 nm in diameter) were chosen so as to reproduce the observed spread of fluorescence and ratio of puff-to-trigger amplitudes. Although the model of calcium release built in this way gave the correct ratio value, it was unable to reproduce the absolute value of the fluorescence (if a linear relationship between fluorescence and Ca^{2+}-bound dye distribution was assumed [1,8]). In the present paper we follow a complementary approach to estimate the properties of Ca^{2+} release during puffs. Namely, we use a "backward method" [9] which starts from the relationship between fluorescence and Ca^{2+}-bound dye distribution and works its way back to obtain the underlying Ca^{2+} current amplitude and kinetics [1].

The quantal properties of Ca^{2+} release during puffs have recently been revealed using total internal reflection fluorescence (TIRF) microscopy [10]. In that paper puffs were observed in intact mammalian cells (human neuroblastoma SH-SY5Y cell line) using membrane-permeant forms of dye and caged IP_3 [11]. The studies of [10] show that the amplitude (in fluorescence) of the observed events occurs in multiples of an elementary amplitude event. The largest amplitudes observed in these cells are of the order of 20 times the elementary amplitude, whereas in most puffs around 6 active IP_3Rs are involved. The observations also show that channel openings are synchronized within 10-20ms, and that the subsequent time course is largely characterized by successive channel closings. Although that paper provides a detailed description of the kinetics of channel openings and closings, it does not give direct quantitative information on the single-channel IP_3R Ca^{2+} current. An approximate estimate was made by comparison with fluorescent signals arising from Ca^{2+} flux through single nicotinic acetylcholine receptor channels [12]. The SH-SY5Y cell line provides an excellent system to study Ca^{2+} puffs, and the method of [10] employing TIRF microscopy gives cleaner records with better resolution than those obtained from *Xenopus laevis* oocytes using confocal microscopy. However, TIRF imaging is less readily applicable to *Xenopus* oocytes owing to the location of puff sites a few micrometers inward from the plasma membrane. We thus sought to derive as much quantitative data as possible from confocal images regarding local Ca^{2+} puffs in the *Xenopus* oocytes, in light of the extensive existing literature on this cell type and in order to make a more quantitative comparison between differing cell types.

Obtaining quantitative results for the calcium flux from the analysis of fluorescent images is not straightforward. Different approaches have been used, particularly for "sparks", which are elementary events of Ca^{2+} release through ryanodine receptors (RyR's) in skeletal and cardiac muscle. In some of these approaches, a detailed model of all the processes is proposed, a complete set of partial differential equations for all the species involved is solved numerically, and the obtained theoretical signal is compared with the experimental one to determine the magnitude of the ionic current [13-16]. Although the simulated signals reported in these works were comparable to the experimental ones and the magnitudes of the fluxes were in good agreement with the expected values, these methods have the great disadvantage that all the numerical parameters that characterize the processes that modulate calcium signals must be known in full detail. In *Xenopus laevis* oocytes, this information is not well known. To overcome this difficulty, in [17,18], we explored the possibility of deriving simple mathematical descriptions directly from the experimental observations. This "data-driven" approach is at the basis of the algorithm to infer the calcium fluxes that underlie fluorescence images which we introduced in [1]. In the present paper, we modify this algorithm using an even simpler "data-driven" model to describe intracellular calcium dynamics which holds in the presence of localized calcium sources and which we tested extensively in [18]. We apply this version of the algorithm to IP$_3$-evoked Ca^{2+} puffs in *Xenopus laevis* oocytes, in the presence of EGTA, and obtain information on the spatiotemporal dynamics of the underlying Ca^{2+} fluxes. In particular, we find that Ca^{2+} release comes from a region of width ~ 450 nm, that the release duration is peaked around 18ms and that the Ca^{2+} currents range between 0.12 and 0.95pA. Considering simple cluster models in which all channels open and close simultaneously, we infer what number and spatial organization of IP$_3$Rs is compatible with the experimental observations analyzed in the present paper and with the puff-to-trigger amplitude distribution reported in [2]. We find that the variability among clusters plays an important role in shaping the observed puff amplitude distribution and that the observations are best fit by a model for which the current, I, scales linearly with the number of channels involved in the event, N_p, for small N_p and sublinearly for large N_p. This simple "mean-field" model provides averaged information. Using a model that includes the stochastic dynamics of the individual channels it is possible to show that the nonlinear behavior of $I(N_p)$ can be attributed to the limited time resolution of the observations and the averaging procedure implicit in the mean-field models.

2. Materials and Methods

2.1. Experiments

Preparation of Xenopus oocytes—*Xenopus laevis* were anaesthetized by immersion in 0.17 % MS- 222 for 15 min and killed by decapitation in adherence with protocols approved by the UC Irvine Institutional Animal Care and Use Committee. Oocytes (Dumont stage V VI) were manually plucked and collagenase-treated (0.5 mg ml^{-1} for 30 min) before storage in Barth's solution (composition (mM): NaCl, 88; KCl, 1; NaHCO3, 2.4; MgSO4, 0.82; Ca(NO3) 2, 0.33; CaCl2, 0.41; HEPES, 5; pH 7.4) containing 0.1 mg ml^{-1} gentamicin at 17 °C before use.

Microinjection of oocytes—Intracellular microinjections were performed using a Drummond microinjector. Oocytes were loaded with either Fluo-4 low affinity dextran (K_d= 4.07 μM: 11 oocytes) or Oregon green BAPTA-1 (K_D= 0.17μM: 1 oocyte), together with caged IP$_3$ (D-myo-inositol 1,4,5- trisphosphate, P4(5)-(1-(2-nitrophenyl)ethyl) ester. Final intracellular concentrations of were 25μM Fluo-4, 40μM Oregon green and 12.5 caged IP$_3$; assuming 1 μl cytosolic volume. An EGTA buffer solution (5 mM EGTA together with 2.5 mM CaCl$_2$; pH 7.25, with KOH) was then injected through a fresh micropipette to obtain final

intracellular concentrations of 300 μM EGTA (for Fluo-4 experiments) or 135μM (for Oregon green experiments).

Confocal laser scanning microscopy—Confocal Ca^{2+} images were obtained using a custom-built linescan confocal scanner interfaced to an Olympus IX70 inverted microscope [19]. Recordings were made at room temperature, imaging in the animal hemisphere of oocytes bathed in normal Ringer's solution (composition (mM): NaCl , 120; KCl, 2; CaCl₂, 1.8; HEPES, 5; pH7.3). The laser spot of a 488 nm argon ion laser was focused with a 40X oil immersion objective (NA 1.35) and scanned every 8 or 2.6 ms along a 50 μm line (0.06 μm/ pixel), in the experiments with Fluo-4 and every 2ms (with 0.15 μm/pixel), in the experiments with Oregon-green. Emitted fluorescence was detected (wavelengths > 510 nm) through a confocal pinhole providing lateral and axial resolutions of about 0.3 and 0.7 μm, respectively. The scan line was focused at the level of the pigment granules and images were collected through a coverglass forming the base of the recording chamber. Fluorescence signals are expressed as ratios ($F_R = F/F_0$) of the fluorescence (F) at each pixel relative to the mean resting fluorescence (F_0) at that pixel prior to stimulation. IP_3 was photoreleased from a caged precursor by delivering flashes of UV light, focused uniformly throughout a 200 μm spot surrounding the image scan line [20]. The amount of photo-released IP_3 was controlled (in a linear manner) by varying flash duration (5-30 ms). Each flash consumes only a negligible fraction of the caged IP_3 [20], thus it was possible to acquire numerous consistent responses using repeated flashes. Intervals of > 60 s were allowed between recordings to allow IP_3Rs to recover from desensitization and for cytosolic $[Ca^{2+}]$ to return to basal levels.

Reagents—Fluo-4 dextran, Oregon green BAPTA-1 and caged IP_3 were from Molecular Probes Inc. (Eugene, OR, USA); all other reagents were from Sigma Chemical Co. (St Louis, MO, USA).

2.2. Processing of experimental signals

The linescan images provide values of Ca^{2+}-dependent fluorescence along a single spatial dimension as a function of time. Thus, we have a matrix of fluorescence values, $F(x_i,t_j)$, at each point, x_i along the line-scan and time, t_j. Fluo-4 experiments yielded images of 1506×443 or 928×776 pixels. Oregon green experiments gave 907×321 pixel images. A typical Fluo-4 image, showing puffs evoked at several sites in response to a 20 ms photolysis flash, is shown in Fig. 1A.

We process the signals according to the following steps:

a. For each image, we compute the ratio:

$$F_R\left(x_i, t_j\right) = \frac{F\left(x_i, t_j\right)}{Fo\left(x_i\right)},$$

(1)

where $Fo(x_i)$ is the average of $F(x_i,t_j)$ over all the times before the flash occurs.

b. Puff identification

Puffs are identified using an automated threshold criterion [21]. First, the data set corresponding to each image is integrated over time and a spatial profile is obtained. Points from this profile for which the fluorescence value exceeds a given threshold are considered as puff site candidates. This selection gives disconnected sets of x values. From each set we keep the value, x_k, of maximum fluorescence over that set. We then repeat the procedure, but working with the spatial average of the original signal. This gives "clusters" of t values from which we keep the times, t_k, at which

the maximum fluorescence occurs for each cluster. Then, we select a 40×50 pixel box around each point, (x_k, t_k). To decide if a box contains a puff or not, we calculate its average fluorescence. If this value is above a given threshold (which we take as $m+a\sigma$, where m and σ are the mean and standard deviation of the fluorescence, F_R and a is equal to 1 or 1.5, depending on the noise level of the data.), we consider that the box contains a puff. This procedure is rapid and efficient. An individual puff, captured from Fig. 1A, is shown in Fig. 1B. Puffs from Oregon green experiments are, on average, noisier than those from Fluo-4 experiments. The automated threshold criterion failed to detect several puffs, therefore we use a semi-automated criterion, as follows. We first determine an approximate puff location, $(x_k, t_k)_{app}$, bye eye inspection and then automatically refine the position of the puff by searching for the maximum fluorescence on a box of 11×61 pixels around $(x_k, t_k)_{app}$.

c. Puff averaging

The algorithm we use to infer the Ca^{2+} flux properties from the experimental data needs the image to be relatively smooth. To this end, we use averaged images, as the one in Fig. 1C, which we obtain in the following way. We first determine the amplitude $A = max(F_R)$, spatial spread l_f and time to peak t_f of the puffs, as explained below. Next, we compute the distance in parameter space between $puff_i$ and $puff_j$ as:

$$d_{ij} = \sqrt{a_1\left(\max(F_R)_i - \max(F_R)_j\right)^2 + a_2\left(l_{f_i} - l_{f_j}\right)^2 + a_3\left(t_{f_i} - t_{f_j}\right)^2},$$

where $a_1=16$, $a_2=400$ and $a_3=1$ are scaling factors. We then replace each puff, $puff_i$, by its average with all other puffs, $puff_j$, such that d_{ij} is smaller than a given tolerance. This average puff image is computed after the puff centers (i.e., the peak locations) are aligned. Typically between 2 and 5 puffs are used for each average. As expected, the resulting averaged puff has lower amplitude than the raw ones. However, the reduction of the puff amplitude is less than 20% and the distributions of the raw and averaged puffs amplitudes are very similar for Fluo-4 experiments (see Supplementary Information). Fig. 1.D shows an example of 5 Fluo-4 puffs that were averaged to obtain a smooth event. The amplitude, rising time and spatial extent of the 5 raw puffs were: A=9.09, 8.11, 8.9, 7.8 and 8.79 t_f=10.4, 15.6,15.6, 17.1 and 18.2ms and l_f=1.5, 1.5,1.44, 1.26 and1.62μm, those of the averaged puff are A=6.5, t_f=13ms and l_f=1.26μm. Finally, each of these averaged puffs is divided in two halves along the spatial coordinate (one half has $x>0$ and the other, $x<0$) and the values of F_R with the same value of $|x|$ and t are further averaged. With this procedure, each puff is replaced by a smoother one that approximately has its same properties. The total number of averaged puffs does not differ significantly from the total number of raw ones: only puffs that are very different from any other puff are left aside. In this way, we could obtain 117 averaged puffs out of 130 raw ones in the case of Fluo-4 experiments. In the case of Oregon green experiments we smoothed out the images by averaging the pixels over a 42ms×800nm region before applying the averaging procedure just described. In this way we obtained 406 averaged puffs after discarding those that qualified as out of focus (see Results). We call $\bar{F}_R$ the resulting averaged fluorescence and $\bar{A}$ the averaged puff amplitude. All the subsequent processing assumes that puffs have spherical symmetry and that the linescan passes through the center of the puff. In this way we can assume that a linescan provides complete information on the signal so that the spherical coordinate, r, (the distance from the puff center) is enough to fully describe the puff. We check the validity of this approximation in the Results Section.

2.3. Determination of puff duration and spatial spread

Typical temporal profiles of puffs at their center ($r = 0$) show that the signal rises rapidly to a maximum value and then decays at a slower rate (e.g. Fig. 1E). To characterize the duration of Ca^{2+} flux during a puff we determine the rise time or t_f taken for the fluorescence signal to increase from a value 1.5 standard deviations above the mean basal value to the peak (Fig. 1E). A similar analysis is done to determine the spatial spread l_f of the signals, defined as the full-width of the fluorescence signal at an amplitude of 60% of the peak at the time of the peak (Fig. 1F). As explained in the following section, we do not apply any deblurring to the image, which may result in a slight overestimation of the puff spatial spread.

2.4. Inferring Ca²⁺ flux properties

Determination of free Ca²⁺ distribution—In order to determine the Ca^{2+}-bound dye concentration, $[CaB]$, we relate it to the fluorescence, assuming that the fluorescence in the absence of calcium, $Fmin$, is negligible for both indicator dyes; *i.e.*, we assume that:

$$[CaB]\left(r_i, t_j\right) = [B]_T \frac{F_R\left(r_i, t_j\right) - \frac{F\min}{Fo(r_i)}}{\frac{F\max}{Fo(r_i)} - \frac{F\min}{Fo(r_i)}} \cong [B]_T \frac{F_R\left(r_i, t_j\right)}{\frac{F\max}{Fo(r_i)}}$$

(2)

Based on the studies reported in [1], we do not apply any deblurring to the image since the procedure introduces too much noise and exaggerates errors if the scan line is offset with respect to the puff center. This can result in a slight overestimation of the puff spread and source size. In the case of experiments with Fluo-4, F_{max}, the fluorescence of Ca^{2+}-saturated dye, was determined by injecting saturating amounts of calcium from a pipette filled with 100 mM $CaCl_2$ into oocytes, yielding a value of $F_{max}/Fo \cong 48$. For a total dye concentration $[B]_T = 25\mu M$, we obtain $[CaB]$ values around 0.5μM at rest, which corresponds to $[Ca^{2+}]_{basal} \sim 80nM$, assuming a $K_D = 4.07\ \mu M$ (with Oregon green, we obtain a value for $[Ca^{2+}]_{basal}$, which is in the same order of magnitude). This is a reasonable value for $[Ca^{2+}]_{basal}$, which we use to confirm that the approximation of Eq. 2 is valid for the experiments analyzed. Values of $[CaB]$ are around 4μM at the peak fluorescence during puffs. Oregon green does not provide a fluorescence range as large as that of Fluo-4. In fact, F_{max}/Fo is an order of magnitude smaller [6]. This results in noisier records experiments with puffs that are harder to detect. We analyzed Oregon green experiments mainly to validate the conclusions we obtained using Fluo-4 as the indicator. For the parameters that characterize Oregon-green we follow [22]; ($D_{dye} = 20\mu m^2 s^{-1}$, $k_{on} = 15\mu M^{-1}s^{-1}$, $K_D = 0.17\mu M$) and take $F_{max}/Fo = 1.6 \sim K_D/[Ca^{2+}]_{basal}$ that gives current values within the range of those obtained in experiments with Fluo-4.

Discrete approximations, L and T, of the Laplacian $\left(\frac{\partial^2}{\partial r^2} + \frac{2}{r}\frac{\partial}{\partial r}\right)$ and of the time derivative $\left(\frac{\partial}{\partial t}\right)$ of $[CaB]$ are computed numerically at every r and t. A first-neighbor smoothing procedure is applied to $[CaB]$ before the derivation is performed [1].

Assuming that the dye, B, only reacts with free Ca^{2+} according to $Ca^{2+} + B \Leftrightarrow CaB$, that the total dye concentration, $[B]_T = [B] + [CaB]$ is uniformly distributed in space, that k_{on} and k_{off} are the reaction rates, and that CaB diffuses with coefficient D_{dye}, we compute the reaction term, $R = k_{on}\left[Ca^{2+}\right]\left([B]_T - [CaB]\right) - k_{off}[CaB]$, at each r and t as: $R = T - D_{dye}L$ from which we obtain the free calcium concentration at every r and t:

$$\left[Ca^{2+} \right] = \frac{k_{\text{off}} \left[CaB \right] + R}{k_{\text{on}} \left(\left[B \right]_T - \left[CaB \right] \right)}$$

(3)

We then compute discrete approximations of the Laplacian and time derivative of $[Ca^{2+}]$, using second and first difference order finite differences, respectively. A first-neighbor smoothing procedure is applied to $[Ca^{2+}]$ before the derivation is performed [1].

Determination of the Ca^{2+} current—Once the free $[Ca^{2+}]$ and its derivatives are obtained, we use the algorithm introduced in [1] to obtain the Ca^{2+} flux underlying the fluorescent puff image. The only difference with respect to the implementation discussed in [1] is that we assume that the sum of all the Ca^{2+} removal terms can be approximated by a linear function of $[Ca^{2+}]$. As analyzed in [18], this assumption is valid in the vicinity of a localized Ca^{2+} source. Thus, we assume that:

$$M \equiv \frac{\partial \left[Ca^{2+} \right]}{\partial t} - D_{Ca} \nabla^2 \left[Ca^{2+} \right] \cong m_R \left[Ca^{2+} \right] + b_R + Q_{ca},$$

(4)

with D_{Ca} the free diffusion coefficient of Ca^{2+}, Q_{Ca} the localized Ca^{2+} source and m_R and b_R parameters to be determined from the experiment [1,18]. Briefly, by plotting M (which is obtained by finite differentiation of $[Ca^{2+}]$) vs $[Ca^{2+}]$ we identify the region of low $[Ca^{2+}]$ ($Q_{Ca}=0$) where the dependence is approximately linear from which we determine m_R and b_R. Extrapolation of this behavior to the source zone leads to the determination of Q_{Ca}. Integration of Q_{Ca} gives the Ca^{2+} current:

$$I(t) = \gamma \int_0^{r_{source}} Q_{Ca}(r, t)\, 4\pi r^2\, dr,$$

(5)

where $\gamma = 1.92 \times 10^{-4}$ pC/(μMμm^3). This integral is very sensitive to the choice of *dr* because the spatial resolution of the experiments is at most of the order of r_{source}. To overcome this problem, we approximate $Q_{Ca}(r,t)$ by a Gaussian in *r* for each *t*. We choose r_{source} as the point for which two successive points of the Gaussian fitting differ by less than 0.01 (Fluo-4 experiments) or 1.5σ (Oregon green experiments).

As an example of how the method deals with the experimental data, Fig. 1G shows a plot of *M* as a function of $[Ca^{2+}]$ for a representative puff from a Fluo-4 experiment. The straight line corresponds to the sum of all the Ca^{2+} removal terms, $m_R [Ca^{2+}] + b_R$, with m_R and b_R obtained by fitting the *M* vs $[Ca^{2+}]$ data points for low Ca^{2+} (see inset). Fig. 1H shows a spatial profile of Q_{Ca} (black circles). The Gaussian fitting of the source is shown with a solid line in Fig. 1H. Integration of the Gaussian fitting using Eq. 5 gives the current time course, shown in Fig. 1I.

Determination of the duration of Ca^{2+} release and the spatial extent of the Ca^{2+} source—We determine the duration of the Ca^{2+} release (t_r) from the temporal profile of the current, I (Fig 1I). We assume that the release starts and ends when the current, I, becomes equal to 1.5 times the standard deviation around the basal value.

The spatial extent of the source (l_r), as explained before, is determined as twice the radius at which two successive points of the Gaussian fitting of the Q_{Ca} spatial profile at the time of the Ca^{2+} flux peak differ by less than 0.01 (see Fig. 1H). Given that we work with the blurred

image, the source size can be slightly overestimated. Therefore, the numbers we obtain should be considered as upper bounds of the actual values.

2.5. Puff models: Ca^{2+} distribution within an IP3R cluster

To interpret the experimental data, we perform a series of numerical simulations of the Ca^{2+} dynamics in a cytosolic medium with molecular buffers and localized Ca^{2+} sources, similar to the one introduced by Shuai et al. in [4]. The model includes the following species: cytosolic calcium (Ca^{2+}), an immobile endogenous buffer (S), a cytosolic Ca^{2+} indicator (B) and an exogenous mobile buffer ($EGTA$) that react according to:

$$Ca^{2+}+X \underset{k_{off-X}}{\overset{k_{on-X}}{\rightleftarrows}} [CaX]$$

(6)

where X represents S, $EGTA$ or B, and k_{on-X} and k_{off-X} are the forward and backward binding rate constants of the corresponding reaction, respectively. We do not include Ca^{2+} pumps because they act on a slower time scale than typical puff durations. We assume that the total concentration of Ca^{2+} dye, mobile and immobile buffer remain constant ($[B]_T$, $[EGTA]_T$ and $[S]_T$, respectively) and that the diffusion coefficient of their free and Ca^{2+} bound forms are equal. Furthermore, we assume that initially all concentrations are homogeneously distributed and in equilibrium among themselves with Ca^{2+} is at basal concentration, $[Ca^{2+}]_{basal}$. Therefore we can calculate $[B]$, $[EGTA]$ and $[S]$ by subtracting the concentration of the Ca^{2+} bound forms to the total concentration. Given these assumptions, the set of partial differential equations that give the spatial and temporal evolution of the concentrations involved in the description is:

$$\frac{\partial \left[Ca^{2+}\right]}{\partial t} = D_{Ca}\nabla^2\left[Ca^{2+}\right] - \sum_{X=S,EGTA,B} R_{CaX}$$

(7.a)

$$\frac{\partial [CaB]}{\partial t} = D_{dye}\nabla^2[CaB] + R_{CaB}$$

(7.b)

$$\frac{\partial [CaEGTA]}{\partial t} = D_{EGTA}\nabla^2[CaEGTA] + R_{CaEGTA}$$

(7.c)

$$\frac{\partial [CaS]}{\partial t} = R_{CaS}$$

(7.d)

where D_{Ca}, D_{dye} and D_{EGTA} are the diffusion coefficients of Ca^{2+}, B and $EGTA$, respectively

and the reaction terms are given by: $\quad R_{CaX}=k_{on-X}\left[Ca^{2+}\right]\left([X]_T - [CaX]\right) - k_{off-X}[CaX]$. The Ca^{2+} entry through

(open) IP$_3$R's is included in the boundary conditions [23]. Namely, we consider the cytosolic space as a parallelepiped of sides L_x, L_y and L_z. The plane $z=0$ represents the surface of the ER membrane, where there are N_s sources of (small) area δS centered at the positions $\mathbf{r}_s(i) = \left(x_s^i, y_s^i, 0\right)$, $i=1,\ldots,N_s$. We assume no flux boundary conditions for all concentrations except for [Ca^{2+}] at the location of the sources, where we consider the condition [23]:

$$-D_{Ca}\frac{\partial}{\partial z}\left[Ca^{2+}\right](\mathbf{r}_s(i) \\ ,t=J_{ch} \quad \text{for} \quad i=1,\ldots,N_s \tag{8}$$

where J_{ch} is the Ca^{2+} flux through the sources. Namely, $J_{ch}=I_{ch}/(2 \cdot F \cdot \delta S)$, where I_{ch} is the single channel current (which is equal to zero if the channel is closed) and F is Faraday's constant ($96,485\ c/mol$).

The simulations are done using a forward Euler method in time and an explicit finite-difference formula in space with a 2nd order expression (first neighbors) for the Laplacian with grid sizes $dx=dy=dz=0.02\ \mu m$ and time step $dt=0.3\ \mu s$. The values of the parameters used in the simulations are listed in Table 1 and coincide with those of [4].

To compare with experimental confocal signals we compute a weighted average of the Ca^{2+}-bound dye concentration, [CaB], as [4]:

$$\left[\bar{CaB}\right](0,0,0,t) = \frac{\int [CaB](x,y,z,t) \times \exp\left(-x^2/\omega_x - y^2/\omega_y - z^2/\omega_z\right)dxdydz}{\int dxdydz} \tag{9}$$

where $\omega_x=\omega_y=0.0325\ \mu m^2$ and $\omega_z=0.231\ \mu m^2$. Inserting it into Eq. 2 we obtain the fluorescence distribution of the simulations which we compare with the experimental data (at the puff center).

In all the simulations the number and location of the channels are chosen beforehand. In most cases, we assume that all the channels open and close at previously established times. We also use the method introduced in [24] to perform some simulations in which the stochastic dynamics of the individual IP$_3$R's is included. To this end, we use a very simple IP$_3$R kinetic scheme:

$$C \xrightarrow{k_{CO} \cdot Ca^{2+}} O \xrightarrow{k_{OI}} I \tag{10}$$

where $k_{CO}=20\ \mu M^{-1}\ s^{-1}$ [25] and $k_{OI} = 100 s^{-1}$ (C$_i$ kinetic model) or $k_{OI}=\tilde{k}_{OI}\left[Ca^{2+}\right]=2.39\left[Ca^{2+}\right]\mu M^{-1}s^{-1}$ (C$_d$ kinetic model). In the latter, $\tilde{k}_{OI}$ has been chosen so that $\tilde{k}_{OI}\left[Ca^{2+}\right]_{\text{mouth}}=1/10ms$ with [Ca^{2+}]$_{\text{mouth}}$ the value of [Ca^{2+}] at the mouth of an isolated open channel as predicted by numerical simulations of a single open channel with a 0.1pA. The scheme is similar to that of [26]. It does not include the IP$_3$ binding and unbinding explicitly but assumes that the fractions of IP$_3$R's with or without IP$_3$ bound are given by an equilibrium relationship. In order to make a sensible comparison with the experiments we smooth out the I(t) profile that we obtain with the stochastic simulations using a moving average with a window of 30 ms.

Verification of the algorithm with simulated data and sensitivity of the inferred currents on parameter uncertainties—As done in [1,18], we have used numerically generated "images" to check that the simplified version of the algorithm that we use in this paper is capable of providing good estimates of the calcium flux. To this end, we simulated the simple model described by Eqs. 7 assuming that there is a single (spherical) Ca^{2+} source at the origin with radius varying from 0.05μm up to 1.0μm and active for a time between 1-15 ms. Applying the algorithm to the "images" obtained with these simulations, we not only obtained a very good value for the current, but we were also able to reproduce the time course and spatial spread of the source fairly well.

The effects of optical blurring owing to the microscope point-spread function, noise and finite resolution were also analyzed using simulated numerical data as described in [1]. Addition of noise at a magnitude comparable to that of the basal noise of averaged experimental records increased the errors with which the current amplitudes were determined (around 30%), but the time course remained well reconstructed (see Supplementary Material).

To test the performance of the algorithm in cases where the dimensions of the Ca^{2+} source are smaller than the pixel resolution, we applied it to numerically generated images obtained with a 0.05μm source and for which the data was saved every 0.1μm at 1ms time-steps (which correspond to typical experimental pixel spacing and time resolutions). Using a Gaussian fitting interpolation to Q_{Ca} to compute the integral in Eq. 5, and choosing r_{source} as the point for which the signal reaches half of the maximum value, we obtained a current that was 20% higher than the input value of the simulation.

The algorithm assumes the *a priori* knowledge of several parameters: the Ca^{2+}-dye reaction constants and the dye and free calcium diffusion coefficients. The dissociation constant, $K_D = k_{off}/k_{on} = 4.07$μM (for Fluo-4), is taken from the manufacturer's data, but the values of the individual rate constants ($k_{on} = 100$μM^{-1}s^{-1} and $k_{off} = 400$s^{-1}, for Fluo-4) and the cytosolic diffusion coefficients ($D_{Ca} = 220$μm^{2}s^{-1}, $D_{dye} = 50$μm^{2}s^{-1}) are less certain. To evaluate the sensitivity of our results to changes in these parameters we generated images numerically using a model with three mobile buffers and one immobile buffer as in [1], and then applied the algorithm using values of D_{Ca}, D_{dye} and k_{on} different from those of the simulations. We explored 114 sets of parameter values taken within the ranges defined in Table 2 and compared the maximum value of the current, I_i, obtained for each set, i, with the one used to generate the numerical image (I_s=1pA). Defining the relative errors as $\Delta E(I_i) = I_i / I_s - 1$ (if $I_i > I_s$) and $\Delta E(I_i) = I_s / I_i - 1$ (if $I_i < I$), and equivalent expressions for D_{Ca}, D_{dye} and k_{on}, we obtained that the errors in the reconstructed current were more sensitive to errors in D_{dye} and k_{on} than in D_{Ca}. Furthermore, the relative error in the current decreased much more when the error in k_{on} decreased than when the errors in the other parameters decreased. Thus, having the correct values for k_{on} first and then, for D_{dye}, seems crucial to obtain good estimates of the underlying current. If we kept the subset for which the relative errors in D_{Ca}, D_{dye} and k_{on} are less than 0.5, the relative error of the current is 0.17 ± 0.03 (mean ± standard deviation, n=23). For the values used in this study this is reached when D_{dye} varies in the range (25-75) μm^2/s, D_{Ca} varies between (160-480) μm^2/s and k_{on} remains between 25 and 180 (μMs)$^{-1}$.

An extended description of these procedures and numerical examples is given in the Supplementary Material.

2.6. Inferring the distribution of the number of channels that open during a puff

We propose very simple models to relate the distribution of open channels with the current distribution and then choose the one that gives the best fit of the observations. As done in [27], we assume that the number of channels that open during a puff is equal to the number of IP$_3$R's with IP$_3$ bound in the cluster and that they all open and close simultaneously (see

Supplementary Section). In this way, the distribution of observed currents, $f_I(I)$, depends on the probability that there are N_p IP$_3$R's with IP$_3$ bound in a cluster, $P(N_p)$, and on the relationship between the current, I, and N_p (the number of channels that open during a puff). We investigate the possibility of reproducing the observed distribution assuming that $P(N_p)$ is a Poisson distribution:

$$P\left(N_p\right)=\frac{m^{N_p}e^{-m}}{N_p!},$$

(11)

where m is the mean number of IP$_3$R's with IP$_3$ bound in a cluster. The underlying assumption here is that all clusters have approximately the same number of IP$_3$R's and that they have similar sensitivities to their agonists so that the mean number of channels that open during a puff is the same for all clusters. As discussed later, we cannot fit the observed $f_I(I)$ very well using Eq. 11. We then relax the assumption that all clusters are similar. For simplicity, we assume that there are discrete cluster populations, each of them characterized by a different mean number of channels, m_i, with IP$_3$ bound:

$$P\left(N_p\right)=\sum_{i=1}^{M}\lambda_i\frac{m_i^{N_p}e^{-m_i}}{N_p!},$$

(12)

where M is the number of distinct cluster populations and λ_i is the fraction of clusters that belong to each population.

Based on previous works, we first analyze if $I(N_p)$ can be approximated by the expression:

$$I\left(N_p\right)=I_0 N_p^{1/\alpha},$$

(13)

with $\alpha=1$ or $\alpha=2$. Taking $\alpha=1$ corresponds to assuming that the Ca^{2+} current is the same through each open channel, regardless of the number of IP$_3$R's that are open [4]. The $\alpha=2$ case corresponds to the results of [7] where the effect of the local [Ca^{2+}] depletion in the lumen of the ER owing to the opening of several closely packed IP$_3$R's was analyzed. Taking into account this observation and the ability to fit the experimentally determined $f_I(I)$ (see Supplementary Information), we also explore the possibility that $I(N_p)$ is a nonlinear function such that I and N_p scale differently depending on N_p. For the sake of simplicity, we approximate $I(N_p)$ by expressions of the form $I_o N_p^{1/\alpha}$ with different values of α depending on N_p. Here we only present the results that correspond to the case with $\alpha=1$ for small N_p and $\alpha=2$ for large N_p:

$$I\left(N_p\right)=\begin{cases} I_{o1}N_p & \text{for} \quad N_p<N_{p1} \\ I_{o2}N_p^{1/2} & \text{for} \quad N_p>N_{p2} \end{cases},$$

(14)

Given that $N_{p2}>1$, I_{o1} corresponds to a single IP$_3$R current, while I_{o2} is only a fitting parameter. We can fit the data from Fluo-4 experiments with $N_{p1}=N_{p2}=N_{pt}$ so that $I(N_p)$ is continuous. However, it is not differentiable, which can result in discontinuities in the current distribution function. Since this is only an approximation, we prefer to leave a gap of current values for which we do not determine the current distribution (see Supplementary Information). Something similar occurs for Oregon green experiments. The region for which we do not determine $I(N_p)$ is relatively small and corresponds to values of I for which $f_I(I)$ is also small.

From all possible combinations of $P(N_p)$ and $I(N_p)$ that can be obtained using Eqs. 11-12, we present here the results of assuming that $P(N_p)$ is given by Eq. 11 and $I(N_p)$ by Eq. 13 (both with $\alpha=1$ and $\alpha=2$) and that $P(N_p)$ is given by Eq. 12 and $I(N_p)$ by Eq. 14. In the first case the distribution of puff currents, $f_I(I)$, reads:

$$f_I(I) = \frac{m^{\left(\frac{I}{I_o}\right)^\alpha} e^{-m}}{\Gamma\left(\left(\frac{I}{I_o}\right)^\alpha + 1\right)} \frac{\alpha}{I_o}\left(\frac{I}{I_o}\right)^{\alpha-1},$$

(15)

where Γ is the gamma function, which, for integer arguments, n, satisfies $\Gamma(n)=(n-1)!$ In the second case, given that most of the data that we obtained for Fluo-4 experiments is concentrated in the region with two apparent peaks (see Fig.3A), we only analyze a model with $M=2$. We also assume that, if there are more populations, their contribution to $f_I(I)$ is negligible in the region where most of the data is concentrated ($I<I_m = 0.57$pA). The current distribution then reads:

$$f_I \cong \lambda_1 f_1 + \lambda_2 f_2, \quad \text{for} \quad I<I_m,$$

(16)

where we approximate f_1 and f_2 by:

$$f_j(I) = \begin{cases} \dfrac{m_j\left(\frac{I}{I_{o1}}\right) e^{-m_j}}{\Gamma\left(\frac{I}{I_{o1}}+1\right)} \dfrac{1}{I_{o1}} & \text{for } I<I_1^*, \\[3ex] \dfrac{m_j\left(\frac{I}{I_{o2}}\right)^2 e^{-m_j}}{\Gamma\left[\left(\frac{I}{I_{o2}}\right)^2+1\right]} \dfrac{2}{I_{o2}}\left(\frac{I}{I_{o2}}\right) & \text{for } I>I_2^*, \end{cases} \quad, j=1, 2.$$

(17)

with $I_1^* = I_{o1} N_{p1}$ and $I_2^*=I_{o2} N_{p2}^{1/2}$. We then use Eq. 15 (both with $\alpha=1$ and $\alpha=2$) or Eqs. 16-17 to approximate the observed distribution of puff current amplitudes (Fig. 3A) and extract the best values of the unknown parameters from the fitting. In the latter, we actually approximate $f_I \cong \lambda_1 f_1$ for $I<I^*$ and $f_I \cong \lambda_2 f_2$ for $I>I^*$ with $I^* = I_{o1} N_{pt} = I_{o2} N_{pt}^{1/2}$, and $N_{p1} = N_{p2} = N_{pt}$ (i.e., with no current gap) to do the fitting. We follow a similar approach in the case of Oregon green experiments but leaving a gap in the values of I ($f_I \cong \lambda_1 f_1$ for $I<I(N_{p1})$ and $f_I \cong \lambda_2 f_2$ for $I> I(N_{p2})$) (see Supplementary Information).

3. Results

We present here the analysis of a series of linescan images containing 130 identified puffs of experiments done using Fluo 4-dextran, which yielded 117 averaged signals. The underlying currents were determined for 105 of these averaged events, using the algorithm described in Section 2.4 with parameter values $k_{off} = 400$s^{-1}, $k_{on} = 100\mu$M^{-1}s^{-1} and $D_{dye}= 50\mu$m^2/s for the dye (low affinity Fluo 4-dextran; $K_D = 4.07\mu$M), and $D_{Ca}=220\mu$m^{2}s$^{\pm1}$ [28] for free calcium. We also analyze puffs coming from experiments done with Oregon-green BAPTA-1. In this case, we identified 440 puffs. After averaging and discarding those that qualified as out of focus (see later), we were left with 406 puffs, for 364 of which we could compute the underlying currents. Some of the currents obtained in this case were larger than the largest value (~1pA) obtained for experiments with Fluo-4. Most of these large currents corresponded to relatively wider puffs coming from images with at least two puffs that were very close to one another. Oregon-green records are noisier and the spatial resolution is worse than Fluo-4 ones. Furthermore, the parameter values of Oregon green are not as well characterized. For all these reasons, the only events recorded with Oregon green included in the present analysis have

currents below 1pA, leaving 266 puffs that we analyze to verify some of the conclusions drawn from Fluo-4 images. To a large extent all the analysis is done in terms of the distributions of puff amplitudes and maximal Ca^{2+} currents, I_{max}, that underlie each averaged puff. The latter is computed, using current bins of size $\Delta = 0.05$pA for Fluo-4 and $\Delta = 0.04$ pA for Oregon green experiments, as:

$$f(I_{\max}) = \frac{N(I_{\max})}{N_{\text{total}}\Delta},$$

(18)

where $N(I_{max})$ is the number of puffs for which I_{max} falls within each bin, and N_{total} is the total number of puffs that are analyzed. The amplitude distributions of raw and averaged puffs (f (A) and $f\left(\bar{A}\right)$, respectively, are computed similarly, using bin sizes $\Delta = 0.71$ and 0.73, respectively, for Fluo-4 experiments and a bin size $\Delta = 0.025$ for Oregon green. The puff amplitude distribution, the time course and spatial extent of puffs and the underlying Ca^{2+} currents are presented in Section 3.1-3.3. A scaling relationship between current and the number of open channels during a puff is presented in Section 3.4. In order to validate our interpretation of the experimental results, we complement our analysis with numerical simulations of Ca^{2+} release from clusters of IP3R's in Section 3.5.

3.1. Puff amplitude distribution

We show in Figs. 2A,B the averaged puff amplitude distributions for Fluo-4 and Oregon green experiments, respectively. In the case of Fluo-4, the distribution is similar to that of raw puffs but is slightly shifted to the left due to the averaging procedure. The magnitude of the shift is less than 12% and the mean values of the raw and averaged data are 7.5 and 6.7, respectively. Taking this correction into account, both distributions do not statistically differ ($p < 0.25$, Kolmogorov-Smirnov (K-S) test [29], see Supplementary material). The time course and spatial spread of the raw and averaged puffs are also very similar (data not shown). We further validate the conclusions that we can draw from the analyses of averaged puffs in the next Section. Thus, from now on we will show results that were obtained using averaged puffs, unless otherwise noted.

Fluo-4 experiments were done for various flash durations. This means that the amount of photoreleased IP_3 may be different for different puffs. We analyzed the puff amplitude cumulative distribution function (CDF) for events evoked by flash durations ranging between 8 and 30ms. The distributions overlapped, revealing that there is no apparent dependence of the measured amplitude on the amount of photoreleased IP_3 (the distributions do not differ with $p < 0.1$ according to the K-S test, see Supplementary material), in agreement with [2, 11]. Thus, all further results were obtained after pooling data with various flash durations, in the case of Fluo-4 experiments.

The amplitude distribution, $f(A)$ obtained from the experiments may be affected by two problems. Firstly, very faint puffs are hard to detect, so that low amplitude events may be underestimated. Secondly, puff amplitudes may be underestimated if the linescan does not go through the center of the puff. Given that out of focus events should give rise to relatively wider and dimmer images than in focus ones, we compared the cumulative amplitude distribution, $F(A) = \int_0^A f(A')\,dA'$, obtained using all observed puffs and the one obtained after having discarded the widest dimmest images and they do not differ with $p < 0.1$ according to the K-S test. We kept all averaged puffs in the case of Fluo-4 experiments and discarded the widest dimmest in the Oregon green case.

3.2. Time course and spatial extent of puffs and underlying Ca^{2+} fluxes

Fig. 2C shows the distribution of puff rise times, t_f, for Fluo-4 experiments. Rise times range between 8 and 60ms, with a mean value around 25ms. On the other hand, the corresponding distribution of release flux durations, t_r (Fig. 2D) has a mean around 18ms, with a range from 5 to 33 ms. We could expect similar distributions for t_f and t_r. However, we found that the fluorescence rise time is longer than the underlying Ca^{2+} release. This discrepancy may arise from the procedure used to compute both magnitudes (see Materials and Methods). In this procedure we use 1.5 times SD from baseline as a threshold criterion: since current profiles are generally noisier than puff profiles, the threshold value could be shielding the beginning of the event in the case of the fluxes. For the sake of comparison, we show in Fig. 2E the distribution of t_r obtained for Oregon green experiments. The distribution of flux durations obtained from Oregon green experiments is spread over a wider range, although all durations remain within the same order of magnitude, 41±17ms. The difference in the duration of flux duration may be due to the extra smoothing procedure we needed to apply to reduce the noise in Oregon green experiments.

Fig. 2F shows the observed distribution of fluorescence spread, l_f, during puffs from Fluo-4 experiments. It can be seen that puffs show a great variability in size ranging from 0.3 to 2.2μm. The marked cutoff at $l_f > 2.2$μm is artifactual, resulting from the choice of box dimensions used to capture the puffs to avoid the overlap of neighboring puffs. Corresponding estimates of the spatial extent of the underlying Ca^{2+} sources, l_r, are plotted in Fig. 2G, showing a tight distribution with a mean 450nm. This value, however, should be considered as an upper bound of the actual size. The distribution of source sizes obtained from Oregon green experiments is mainly concentrated around ~400nm (470±120nm) as shown in Fig. 2H. However, there is a large size tail comprising 15% of the events. The discrepancy with respect to Fluo-4 experiments may be due to the different spatial resolutions of both types of experiments. The extra smoothing procedure that we needed to apply to the records coming from Oregon green experiments may also be the reason for the difference in the distributions of l_r.

In order to test to what extent the determined values of t_r and l_r are compatible with the observed t_f and l_f values, we numerically simulated Eqs. 7 assuming that there was a single (spherical) Ca^{2+} source at the origin, that released Ca^{2+} with a constant current, I_{max}, that remains on during a time, t_r. We performed a series of simulations varying t_r, I_{max}, and the source spatial extent, l_r, compatible with the ones obtained from the analysis of Fluo-4 experiments. We then computed the fluorescence distribution according to Eq. 2 using the blurred version of the numerically determined Ca^{2+}-bound dye distribution, Eq. 9. We compared this numerically determined fluorescence with the experimental puff image for which we obtained similar values of t_r, I_{max}, and l_r as those used in the simulations, and we obtained values that differed in less than 20% (not shown). We also performed a numerical simulation using $I_{max} = 0.4$pA, $l_r = 230$nm, and $t_r = 18$ms, which correspond to the mean values of these quantities over all the puffs that we analyzed. The numerically determined puff, in this case, has a spatial spread of 1.3μm, which is within the size values of the observed puffs. These comparisons provide both a validation of the algorithm and of the puff averaging procedure.

3.3. Magnitudes of Ca^{2+} currents during puffs

We show in Fig. 3A the distribution of inferred peak Ca^{2+} currents, $f(I_{max})$ underlying the averaged puffs of type I experiments. Current amplitudes vary between 0.12 and 0.95 pA, with a mean of 0.34 ± 0.2 pA (n=105). Fig. 3B shows the dependence of the averaged puff amplitudes, as a function of current amplitude, I_{max}, for Fluo-4 experiments. The relationship between A and I_{max}, is nonlinear. The saturation of A with increasing I_{max} is also compatible with the results of Thul and Falcke [7]. In that paper the authors simulated the currents and

concentration profiles generated by the release of Ca^{2+} from the endoplasmic reticulum through clusters of IP_3R's. Their Fig. 7, for example, shows that, at the center of the cluster, $[Ca^{2+}]$ is an increasing nonlinear function of the number of open channels, which saturates and eventually starts to decrease as the number of open channels increases. This happens for all the simulations, which correspond to different ratios of mobile to immobile buffer concentrations in the reticulum. In agreement with [7], the current is also an (increasing) nonlinear function of the number of open channels (see their Fig. 7). We discuss later the causes of this behavior. We show in Fig. 3C the distribution of inferred currents for Oregon green experiments.

The algorithm to infer the Ca^{2+} current associated with an event relies heavily on the assumption that the linescan goes through the puff center. As analyzed in [1], the Ca^{2+} flux is underestimated if this assumption does not hold. In [30] an algorithm to go from the distribution of observed amplitudes to the distribution of actual (in focus) amplitudes in the case of sparks was introduced. As mentioned by the authors, the algorithm gives a real amplitude distribution only under the assumption that all the signals (sparks) generate Gaussian fluorescence distributions with the same standard deviation, an assumption that most likely does not hold for puffs. The issue of to what extent the observed puff amplitude distributions, $f_A(A)$, reflect that of the underlying currents that generate the observations, $f_I(I)$, was addressed in [31], where the authors introduced the observation function, $g(I,h)$ to relate A, I and the line-scan offset, h. Unfortunately, there is no method to obtain this observation function directly from the experiments. Furthermore, both the methods of [30] and [31] use statistical arguments to go from the observed to the real distribution, something that is not good for our purposes since our algorithm works with each puff individually, for which we would need to know the offset in each case. Therefore, as done before, taking into account that out-of-focus events should give rise to relatively wider and dimmer images than in-focus ones, we compared (in the case

of Fluo-4 experiments) the cumulative current distribution, $F(I) = \int_0^I f(I')\,dI'$, obtained using all the determined currents (a total of 105) and the one obtained using the currents that corresponded to the 51 narrowest puffs. The Kolmogorov statistics, $T \equiv \sup_x |F_1(x) - F_2(x)|$, determined that both distributions did not differ with an 80% statistical significance [29]. In addition, using "numerical simulated images" as described in the above section, we compared 32 puffs coming from both distributions and the numerically generated fluorescence distribution differed by less than 20% with respect to the experimental ones, independently if they were narrow and intense or not. We then assume that out of focus events are not affecting the current distribution that we could obtain significantly in the case of Fluo-4 experiments. We thus work with the distribution function obtained using all the 105 currents that we could obtain in this case. For Oregon green experiments we discard the information coming from the 8 widest, dimmest events.

Fig. 4 shows the flux duration and the size of the underlying Ca^{2+} sources as functions of the inferred maximum current, I_{max} for Fluo-4 and Oregon green experiments. None of these parameters showed any appreciable dependence on the underlying current, although a weak increasing dependence may be observed in Fig. 4C. We arrive at the same conclusion if we only analyze a subset of puffs, *e.g.*, those with amplitudes larger than the value at which $f(A)$ has its maximum [31]. The discarded events in the latter comprised around 20% of the total number of puffs, in the case of Fluo-4 experiments. Oregon green experiments show a much larger variability both in t_r and l_r. Although the size of the source seems to increase with the current I>0.6 pA, the data in that region are not sufficient to draw a definitive conclusion (Fig. 2H and 3C).

3.4. Relationship between current and number of open channels

We show in Fig. 5A the current distribution of Fig. 3A (Fluo-4 experiments) with bars and the results of approximating it by Eq. 15 (dashed curves) with $\alpha=1$ and $\alpha=2$. We show a similar plot in Fig. 5D but for Oregon green experiments. For Fluo-4, the fitting gives $I_o=0.086$pA and $m=4$ for $\alpha=1$ and $I_o=0.45$pA and $m=0.72$ for $\alpha=2$. For Oregon green, $I_o=0.19$pA and $m=1.2$ for $\alpha=1$ and $I_o=0.14$pA and $m=13$ for $\alpha=2$. None of the theoretical distributions seems to be a good representation of the experimental data. Furthermore, in the $\alpha=2$ case, the mean number of open channels, m, and the single channel current, I_o, for Fluo-4 experiments are quite unrealistic.

We show in Fig. 5C the result of approximating the observed Fluo-4 distribution by Eqs.16-17 (up to I_m). The fitting gives $I_{o1} = 0.017$ pA, $m_1=15$, $I_{o2} = 0.08$pA, $m_2 = 33$, $\lambda_1= 0.71$, $\lambda_2= 0.27$ and $I^*=0.38$pA. As expected, each population of IP$_3$R clusters is characterized by a different mean number of channels that open during a puff, m. We show the corresponding function $I(N_p)$ (Eq.15) in Fig. 5C. The current that guarantees the continuity of $I(N_p)$ which we used for the fitting, $I^*=0.38$pA, practically coincides with the value at which the current distribution has a minimum. Small variations in the value I^* that we used did not alter the parameter values of the theoretical distribution too much. We show similar plots for Oregon green experiments in Figs.5E-F. The parameters in this case are: $I_{o1} = 0.025$ pA, $m_1=4.72$, $I_{o2} = 0.107$pA, $m_2 = 23.6$, $\lambda_1= 0.71$, and $\lambda_2= 0.11$. In this case we kept a gap (the region between 0.26 and 0.43pA where I switches from the $\sim N_p$ to the $\sim N_p^{1/2}$ scaling) to do the fitting. We observe that a change of scaling from $I \sim N_p$ to $I \sim N_p^{1/2}$ and a single channel current $I_{o1} \sim 0.02$ pA are compatible with the observations from Oregon green experiments. The distribution defined by Eqs.16-17 seems to approximate the observed current distribution better than Eq.15. However, it involves many more parameters and it is not evident which distribution is the most likely.

We also tried to fit the data assuming a single scaling relationship between I and N_p for the whole range of observed currents ($\alpha_1 = \alpha_2= 1$), but two cluster populations. Namely, we considered that $I(N_p)$ was given by Eq. 13 with $\alpha=1$ and that $P(N_p)$ was given by Eq. 12 with $M=2$. The values obtained in this way for Fluo-4 experiments were very unreasonable (e.g., $I_o = 0.0038$pA and $m_2 = 118$) and we do not show these results here. It is also possible to fit the distribution assuming that $P(N_p)$ is given by Eq. 12 with $M=2$ and that $I(N_p)$ is given by Eq. 13 with $\alpha=1$, but with a different value of I_0 for each population. In particular, for the second population we obtain $I_{02}=0.008$pA and $m_2 = 57$, which are unrealistic numbers. For this reason, we do not discuss these models here.

3.5. Numerical simulations and comparison with other experimental observations

One may argue that the quality of the fit is better using Eqs.16-17 than using Eq.15 (with $\alpha=1$) only because there are more fitting parameters in the former model. To choose between them, we first applied the Akaike (AIC) and Bayesian (BIC) information criteria (in the case of Fluo-4 experiments). The AIC criterion favored the model given by Eqs.16-17 while the BIC criterion favored the other one. Taking this result into account and considering that the puff amplitude and current distributions may not be a faithful representation of the whole set of events that occur in the cell given that very dim puffs could go undetected, we decided to compare the predictions of the models by means of numerical simulations. To this end, we simulated the Ca^{2+} distribution in the presence of different numbers of open IP$_3$R's and different choices of the single channel current as described in Sec. 2.5. Based on the results of Fig. 2G, we distributed the open channels randomly over a 0.5 μm × 0.5 μm square, as shown in Fig. 6B. We picked the channel locations among the nodes of a square grid of 20nm sides and discarded the configurations for which the inter-channel distance was less than 56nm. For the single channel current, we either chose a constant value, $I_{ch}=I_o=0.086$pA, (the one we obtained from the fitting of Fluo-4 experiments under the assumption that $f_I(I)$ is given by Eq. 15 with $\alpha=1$)

or a value that depended on the total number of open channels, N_p, so that N_pI_{ch} was given by Eq. 14 (the relationship that underlies Eq. 17).

First we checked whether the two models could reproduce the puff amplitude to current relationship displayed in Fig. 3B. To this end we performed the simulations assuming that all the channels became open at the same time and remained open for 18 ms. We then computed the blurred version of the Ca^{2+}-bound dye distribution given by Eq. 9 and the corresponding fluorescence amplitude with Eq. 2. The results are displayed in Fig. 3B (open circles for the model with constant $I_{ch}=I_o$=0.086pA and solid circles for the model for which N_pI_{ch} is given by Eq. 14). We used N_p=1,3,5,10,15 for the model with constant I_{ch} which gives a total current between 0.086pA and 1.29pA. Instead, the total current varies between 0.017 and 0.57pA (N_p =1,3,5,10,15,20,25,30,40,50) when we use the model for which N_pI_{ch} is given by Eq.14. Given that there is no noise added to the simulations, based on this comparison we conclude that both models give good representations of the observations.

We then investigated what puff-to-trigger amplitude distribution they gave rise to comparing them with the results reported in [2]. It is worth mentioning that the puff-to-trigger amplitude distribution should not be affected much by offsets of the linescan. To this end, we performed a series of simulations where a certain number - 1, 2 or 3 - of triggering channels opened at t=0 while the rest opened at t=12ms. All the channels closed at t=31ms. A total of N_p channels were open during the puff, which was chosen to last for 19ms. One of the triggering channels was always placed at the center of the cluster. The rest of the channels that opened during the trigger, and those that gave rise to the puff, were distributed randomly over a 0.5 μm × 0.5 μm region. In Fig. 6B we show three examples of the spatial distribution of the channels during a puff with N_p = 5, 30 and 50 open channels. We obtained the best results for 3-channel triggers. In Fig. 6C we show traces of the fluorescence ratio, F_R, for four different simulations of paired trigger-puff events with a 3-channel trigger. The upper traces correspond to simulations in which the single channel current was $I_{ch}=I_o$=0.086pA, independent of N_p, while the other two correspond to $N_pI_{ch}=I$, with I given by Eq. 14. We calculated the amplitude of the puff as F_R at t=0.031s and the amplitude of the trigger as F_R at t=0.012s. In this way we found the puff-to-trigger amplitude ratio for different numbers of open channels during the puff. Assuming that the distribution of open channels is given by Eq. 11 with m=4 or by Eq.12 with M=2, m_1=15, m_2 = 33, λ_1= 0.71 and λ_2= 0.27 (parameters that were obtained from the fitting of Fluo-4 experiments assuming that $f_I(I)$ was given by Eq. 15 with α=1 and Eqs.16-17, respectively) we could further calculate the expected distribution of puff-to-trigger amplitude ratios for both cases. In Fig. 6D we show these distributions together with the experimental distribution reported in [2] (bar plot). We observe that the model that underlies Eqs.16-17 is able to reproduce the experimental puff-to-trigger amplitude distribution fairly well, if we assume that the trigger corresponds to the opening of three channels. The simple Poisson model described by Eq. 11 with m=4 and α=1 fails to reproduce these observations.

4. Discussion

We have applied a "backward method" to infer the properties of Ca^{2+} release during puffs observed in *Xenopus Laevis* oocytes. Backward methods start from the image and perform a series of computations to determine the underlying Ca^{2+} current. Previous works have relied on forward methods in which a model of intracellular Ca^{2+} dynamics is used to generate numerically simulated images that are then compared with experimental ones. Whether forward or backward, most methods that have been used to infer information on the amplitude and kinetics of the Ca^{2+} current that underlies an image require a working model of the cytosolic Ca^{2+} dynamics. This implies the knowledge of a large number of parameters, not all of which can be extracted from the analyzed experiments. The method that we have used requires a minimum of *a priori* assumptions and constructs the model of Ca^{2+} dynamics from the

observations themselves. Using our method we determined the kinetics and amplitude of the calcium current and the size of the calcium release region. Previous estimates of puff calcium currents obtained directly from experiments were based on signal mass calculations that used a rough estimate of how much calcium was bound to the dye compared to endogenous buffers [6]. These calculations gave currents that ranged between 0.4 and 2.5pA. Forward modeling efforts used puff currents that ranged from 0.015pA to 0.8pA [7] or concluded that a good correspondence with experiments could be obtained by assuming the synchronous opening of 25-35 IP3Rs and a single channel current between 0.2 and 0.5pA [4].The application of our method to over 500 puffs gave currents between 0.12 and 0.95pA. The study also showed that the release duration is peaked around 18ms and that the size of the release region ~450 nm does not change much from site to site. This implies that larger puffs correspond to larger densities of channels within the cluster, a result that has implications on signaling since the distance between channels affects inter-channel communication and the ability of signals to propagate. The relatively narrow distribution of source dimensions does not prevent puffs from showing a great variability in extent with sizes ranging from 0.3 to 2.2μm. Numerical simulations in which all channels opened and closed simultaneously showed that having a relatively invariant size of the Ca^{2+} release region is consistent with having puffs of different sizes and that the averaging procedure that we apply to the experimental data does not affect this value significantly. This value, however, could be slightly overestimated (due to blurring) and should be considered as an upper bound for the actual size of the calcium release region. Nevertheless, it is consistent with the estimate of IP3R cluster sizes suggested in [4] (300-800 nm) and with the one determined in [10], which is bigger than those presented in [32,33] (~100 nm).

We studied whether there was a correlation between the duration and the amplitude of the calcium released. As shown in Figs. 4A and 4C and in agreement with [33], the duration of the release and the maximum current amplitude are relatively independent, although a weak increasing dependence can be observed in Fig. 4C. The increasing behavior seems to be contradictory with the inhibitory role that a large $[Ca^{2+}]$ can exert on IP3R's. This apparent contradiction can be understood in terms of the stochastic model described in Sec. 2.5 some of which results we show in Fig. 7. Fig. 7A is a plot of puff duration as a function of puff amplitude for the experiments (open circles) and for the stochastic simulations performed with the C_d IP3R kinetic model (black squares and error bars) and a 0.1pA single channel current. Simulations performed with the C_i kinetic model give similar results. In both the experiments and in the stochastic simulations, the puff duration decreases with the amplitude. This occurs because the larger the maximum current the shorter is the time to achieve the peak current so that t_f is shorter too. For example, a simulated puff with a 3pA maximum current achieves its peak current at 6.5ms and t_f=10.6ms while another puff with a maximum current of 0.9pA achieves its peak current at 16.6ms and t_f=29.8ms. This different behavior may be understood in terms of the spatial organization of the channels involved. The stochastic simulations have been done assuming that the spatial extent of the IP3R clusters is constant regardless of the number of channels that they contain. Thus, the simulated puffs that involve more open channels and have larger amplitudes occur in clusters where the mean distance between available channels is shorter so that CICR occurs on a faster time-scale and the peak current is achieved within a shorter time. This decreasing behavior does not mean that a similar relationship holds between release duration and Ca^{2+} current. This is apparent in Fig. 7B where we show the release duration as a function of the maximum Ca^{2+} current for the stochastically simulated puffs obtained using model C_d (black circles) and C_i (open circles). The maximum current in this case is computed over a smoothed out version of the simulated current that is obtained applying a 20 ms moving average. We observe that the mean value of the release duration increases very rapidly as a function of the maximum current and then reaches a plateau. Thus, the apparent independence observed in the experiments may be attributed to the finite time resolution of the observations. In agreement with this, a nonlinear increasing dependence

between puff duration and maximum number of open channels was observed in experiments with a higher time resolution in which the puff duration is roughly equivalent to release duration [10].

We analyzed to what extent the determined current distribution, $f_I(I)$, was compatible with various underlying distributions of number of open channels, $P(N_p)$, and relationships between I and N_p. In particular, we compared in detail two models. In the first one, $P(N_p)$ was given by Eq. 11 (a Poisson distribution) and $I = Io \, N_p$, so that the current distribution was given by Eq. 15. In the second one, $P(N_p)$ was the superposition of two Poisson distributions (Eq.12 with M=2) and I was given by Eq. 14, so that the current distribution was given by Eqs.16-17. By fitting the experimental data we obtained the various parameters of the models. In particular, the single channel current was I_o=0.086pA in the first model and, in the second one, I_{o1} = 0.017pA when only one channel was open, while it decreased nonlinearly with the number of open channels (giving $I \sim N_p^{1/2}$) when this number was large enough. The nonlinear scaling and the single channel current of the latter agrees with the estimates of [7]. In order to choose between the models, we first applied two information based criteria (AIC and BIC) and each of them favored a different model. In order to overcome this difficulty and the one derived from the possible inaccuracy of the experimental puff amplitude distribution in the low amplitude region, we performed a series of numerical simulations of intracellular Ca^{2+} dynamics in the vicinity of a cluster of IP$_3$R's in which the number and location of the channels that opened during the event were chosen *a priori*. In some simulations all the channels opened simultaneously and, in others, a few channels (a "trigger") opened first and were subsequently followed by the rest. We repeated all the simulations for both types of single channel current. We could reproduce the experimentally determined amplitude *vs* current relationship reasonably well in both cases (Fig. 3B), but for very different values of the number of open channels. When we tried to reproduce the puff-to- trigger amplitude distribution of [2], the model that corresponds to Eqs.16-17 performed much better than the one obtained using Eq. 15 with α=1. We concluded that the model of Eqs.16-17 gives a better description of the experimental observations than the model of Eq. 15 with α=1. This implies, on one hand, that the variability among clusters plays an important role in shaping the puff amplitude distribution that is observed experimentally, which agrees with the findings of [10]. Another distinctive feature of the model that underlies Eqs.16-17 is the nonlinear scaling between the current and number of open channels. This feature could be attributed to luminal Ca^{2+} depletion as discussed in [7]. However, we must remember that the two models that we are comparing here assume that all channels open and close simultaneously. In that respect, they are mean-field models that give "averaged" information. When we drop this simplification and allow the individual channels to open and close stochastically as described in Section 2.5, the experimental observations may be reproduced with the same intra-cluster spatial organization as the one considered in the mean-field models analyzed in Sec. 3.5 but with a different combination of single channel current and number of available channels. In particular, the stochastic model reproduces the observations using any of the two kinetic IP$_3$R models, a fixed single channel current, $I_{ch} \sim 0.1$pA (similarly to the averaged model that underlies Eq. 15) and a number of available channels, N_p, within the range of the averaged model that underlies Eqs. 16-17, as shown in Fig. 7C. This figure displays the results of 474 stochastic simulations performed with the C_d kinetic model for each value of N_p. We show with open circles the maximum released currents as functions of the number of available channels for the stochastic simulations. In order to compare these results with those of the mean field models we computed the average of the Ca^{2+} current released during the whole puff duration for each simulation. We plot the mean (black dots) and standard deviation (vertical lines) of this average as functions of the number of available channels. From the average, which can be approximated as $I \sim N_p$ for small N_p and as $I \sim N_p^{1/2}$ for large N_p, as shown in Fig. 7C, it is possible to compute an effective single channel current, $I_{eff} = I_{ave}/N_p$ that is of the same order of magnitude as that of the model that underlies Eqs.16-17. This is an indication that the nonlinear relationship between

current and number of available channels that we inferred from the observations could be a consequence of having used a mean field model. We will explore the limitations of mean field models elsewhere in more detail. In any case, even if the mean field model that underlies Eqs. 16-17 may not necessarily provide an accurate description of all intra-cluster properties, it can still be preferred, due to its simplicity, over more detailed models as the building block with which to describe more global signals, such as waves.

Finally, we caution that the quantitative information that we extract from the observations is highly sensitive to uncertainties in a priori assumptions of some parameters.. With the aid of simulated models, we have found that good estimates (error less that 20%) of the current amplitudes can be obtained if the uncertainties in the dye diffusion coefficient and the on and off rate constants of the calcium-dye reaction are less than 50%. These results and others [14], [34] point to the necessity of having a good determination of these parameter values for each experimental condition to get reliable results.

Supplementary Material

Refer to Web version on PubMed Central for supplementary material.

Acknowledgments

References

1. Ventura AC, Bruno L, Demuro A, Parker I, Dawson SP. A model-independent algorithm to derive Ca2+ fluxes underlying local cytosolic Ca2+ transients. Biophys J 2005;88:2403–21. [PubMed: 15681645]

2. Rose HJ, Dargan S, Shuai J, Parker I. 'Trigger' events precede calcium puffs in Xenopus oocytes. Biophys J 2006;91:4024–32. [PubMed: 16980363]

3. Callamaras N, Parker I. Radial localization of inositol 1,4,5-trisphosphate-sensitive Ca2+ release sites in Xenopus oocytes resolved by axial confocal linescan imaging. J Gen Physiol 1999;113:199–213. [PubMed: 9925819]

4. Shuai J, Rose HJ, Parker I. The number and spatial distribution of IP3 receptors underlying calcium puffs in Xenopus oocytes. Biophys J 2006;91:4033–44. [PubMed: 16980372]

5. Swillens S, Dupont G, Combettes L, Champeil P. From calcium blips to calcium puffs: theoretical analysis of the requirements for interchannel communication. Proc Natl Acad Sci U S A 1999;96:13750–5. [PubMed: 10570144]

6. Sun XP, Callamaras N, Marchant JS, Parker I. A continuum of InsP3-mediated elementary Ca2+ signalling events in Xenopus oocytes. J Physiol 1998;509(Pt 1):67–80. [PubMed: 9547382]

7. Thul R, Falcke M. Release currents of IP(3) receptor channel clusters and concentration profiles. Biophys J 2004;86:2660–73. [PubMed: 15111387]

8. Smith, GD.; Pearson, JE.; Keizer, J. Modeling Intracellular Calcium Waves and Sparks. In: Fall, CP.; Marland, ES.; Wagner, JM.; Tyson, JJ., editors. Computational cell biology. Springer; New York: 2002.

9. Rios E, Brum G. Ca2+ release flux underlying Ca2+ transients and Ca2+ sparks in skeletal muscle. Front Biosci 2002;7:d1195–211. [PubMed: 11991852]

10. Smith IF, Parker I. Imaging the quantal substructure of single IP3R channel activity during Ca2+ puffs in intact mammalian cells. Proc. Natl. Acad. Sci. U.S.A 2009;106:6404–6409. [PubMed: 19332787]

11. Smith IF, Wiltgen SM, Parker I. Localization of puff sites adjacent to the plasma membrane: functional and spatial characterization of Ca2+ signaling in SH-SY5Y cells utilizing membrane-permeant caged IP3. Cell Calcium 2009;45:65–76. [PubMed: 18639334]

12. Demuro A, Parker I. "Optical patch-clamping": single-channel recording by imaging Ca2+ flux through individual muscle acetylcholine receptor channels. J Gen Physiol 2005;126:179–92. [PubMed: 16103278]

13. Blatter LA, Huser J, Rios E. Sarcoplasmic reticulum Ca2+ release flux underlying Ca2+ sparks in cardiac muscle. Proc Natl Acad Sci U S A 1997;94:4176–81. [PubMed: 9108125]

14. Rios E, Stern MD, Gonzalez A, Pizarro G, Shirokova N. Calcium release flux underlying Ca2+ sparks of frog skeletal muscle. J Gen Physiol 1999;114:31–48. [PubMed: 10398690]

15. Soeller C, Cannell MB. Estimation of the sarcoplasmic reticulum Ca2+ release flux underlying Ca2 + sparks. Biophys J 2002;82:2396–414. [PubMed: 11964229]

16. Baylor SM, Hollingworth S, Chandler WK. Comparison of simulated and measured calcium sparks in intact skeletal muscle fibers of the frog. J Gen Physiol 2002;120:349–68. [PubMed: 12198091]

17. Ventura AC, Bruno L, Dawson S. Ponce. Probing a reduced equation for intracellular calcium dynamics. Physica A: Statistical Mechanics and its Applications 2004;342:281–287.

18. Ventura AC, Bruno L, Dawson SP. Simple data-driven models of intracellular calcium dynamics with predictive power. Phys Rev E Stat Nonlin Soft Matter Phys 2006;74:011917. [PubMed: 16907137]

19. Parker I, Callamaras N, Wier WG. A high-resolution, confocal laser-scanning microscope and flash photolysis system for physiological studies. Cell Calcium 1997;21:441–52. [PubMed: 9223680]

20. Callamaras N, Parker I. Caged inositol 1,4,5-trisphosphate for studying release of Ca2+ from intracellular stores. Methods Enzymol 1998;291:380–403. [PubMed: 9661160]

21. Cheng H, Song LS, Shirokova N, Gonzalez A, Lakatta EG, Rios E, Stern MD. Amplitude distribution of calcium sparks in confocal images: theory and studies with an automatic detection method. Biophys J 1999;76:606–17. [PubMed: 9929467]

22. Baran I. Characterization of local calcium signals in tubular networks of endoplasmic reticulum. Cell Calcium 2007;42:245–60. [PubMed: 17240446]

23. Smith GD, Dai L, Miura RM, Sherman A. Asymptotic Analysis of Buffered Calcium Diffusion near a Point Source. SIAM Journal on Applied Mathematics 2001;61:1816–1838.

24. Solovey G, Fraiman D, Pando B, Dawson S. Ponce. Simplified model of cytosolic Ca2+ dynamics in the presence of one or several clusters of Ca2+ -release channels. Phys Rev E Stat Nonlin Soft Matter Phys 2008;78:041915. [PubMed: 18999463]

25. De Young GW, Keizer J. A single-pool inositol 1,4,5-trisphosphate-receptor-based model for agonist-stimulated oscillations in Ca2+ concentration. Proc Natl Acad Sci U S A 1992;89:9895–9. [PubMed: 1329108]

26. Groff JR, Smith GD. Calcium-dependent inactivation and the dynamics of calcium puffs and sparks. J Theor Biol 2008;253:483–99. [PubMed: 18486154]

27. Fraiman D, Pando B, Dargan S, Parker I, Dawson SP. Analysis of puff dynamics in oocytes: interdependence of puff amplitude and interpuff interval. Biophys J 2006;90:3897–907. [PubMed: 16533853]

28. Allbritton NL, Meyer T, Stryer L. Range of messenger action of calcium ion and inositol 1,4,5-trisphosphate. Science 1992;258:1812–5. [PubMed: 1465619]

29. Conover, WJ. Practical nonparametric statistics. Wiley; New York: 1999.

30. Rios E, Shirokova N, Kirsch WG, Pizarro G, Stern MD, Cheng H, Gonzalez A. A preferred amplitude of calcium sparks in skeletal muscle. Biophys J 2001;80:169–83. [PubMed: 11159393]

31. Izu LT, Wier WG, Balke CW. Theoretical analysis of the Ca2+ spark amplitude distribution. Biophys J 1998;75:1144–62. [PubMed: 9726917]

32. Falcke M. On the role of stochastic channel behavior in intracellular Ca2+ dynamics. Biophys J 2003;84:42–56. [PubMed: 12524264]

33. Shuai JW, Jung P. Stochastic properties of Ca(2+) release of inositol 1,4,5-trisphosphate receptor clusters. Biophys J 2002;83:87–97. [PubMed: 12080102]

34. Shuai J, Parker I. Optical single-channel recording by imaging Ca2+ flux through individual ion channels: theoretical considerations and limits to resolution. Cell Calcium 2005;37:283–99. [PubMed: 15755490]
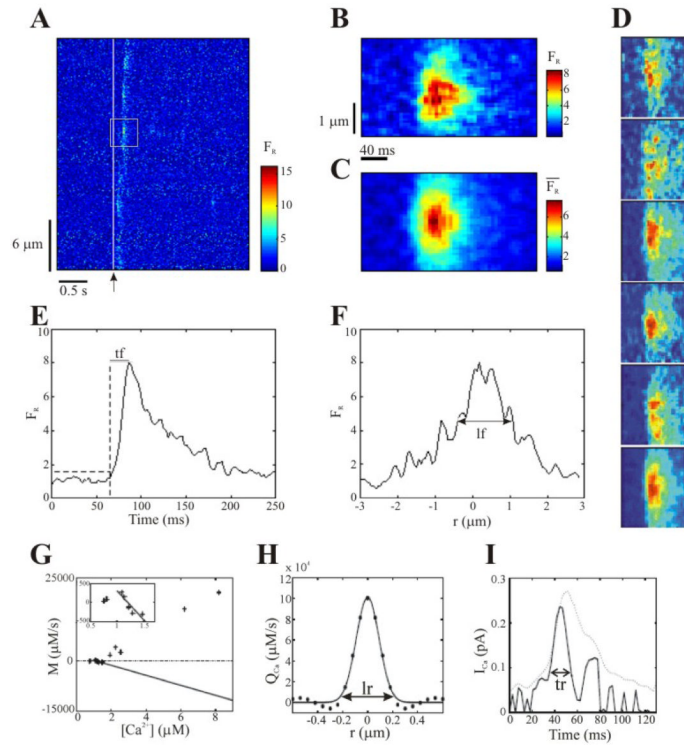
Figure 1.
A. Representative linescan image showing puffs evoked at multiple sites in a *Xenopus laevis* oocyte following photorelease of IP₃ by a 20 ms flash of UV light delivered when marked by the arrow. The oocyte was loaded with EGTA to a final intracellular concentration of 300μM B. Spatiotemporal distribution of F_R obtained from one of the puffs in A (marked by black box), shown on expanded spatial and temporal scales. C. Similar to B, illustrating the averaged fluorescence, $\bar{F}_R$ derived from 3 puff events. D. Averaging procedure. Five raw puffs (first 5 images from top to bottom) and the one obtained using the averaging procedure (lowest image) as described in Materials and Methods. The mean values of puff amplitude, rising time and size are: 8±2, 15±3ms and 1.5±0.2μm for the raw puffs and: 6.5, 13ms and 1.26μm for the averaged one. E, F. Temporal and spatial profiles, respectively, of the puff shown in B, illustrates the measurements of t_f and l_f. G. M as a function of [Ca²⁺] for a representative puff. The filled line represents the extrapolated linear removal. Inset: enlarged view of the main plot for low [Ca²⁺]. H. Spatial profile of the source at the time of maximal signal. Circles: experimental data; solid line: Gaussian fit. l_r is defined as shown. I. Solid line: current time course obtained from the integration of the Gaussian fit to Q_{Ca} and the definition of t_r. Dotted line: the corresponding fluorescence profile (times a constant) at r=0.
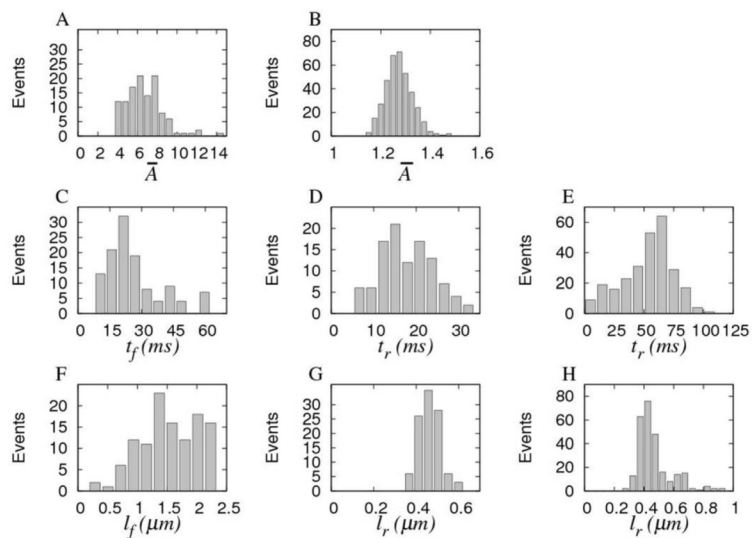
Figure 2.
A,B. Normalized distributions of peak fluorescence amplitude of averaged puffs for Fluo-4 (n = 117) and Oregon green (n=406) experiments. C. Distribution of rise times t_f for Fluo-4 experiments. D, E Distributions of Ca^{2+} flux durations t_r for Fluo-4 and Oregon green experiments, respectively. F-H: Similar to C-E, but for puff (l_f) and Ca^{2+} source (l_r) sizes.
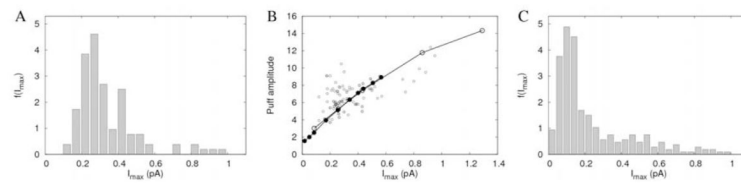
Figure 3.
A. Maximum current value distribution from 105 averaged puffs of Fluo-4 experiments. B. Dependence of puff amplitude on the maximum current during release (Fluo-4 experiments). Black circles correspond to simulations of the model described in Section 2.5 in which the number of open channels was $N_p=1, 3, 5, 10, 15, 20, 25, 30, 40$ and 50 and the single IP$_3$R current I_{ch} was given by Eq. 13 while white circles correspond to simulations with $N_p=1, 3, 5, 10, 15$ and a constant IP$_3$R current of $I_{ch}=0.086$ pA. All channels open during 18 ms. C. Similar to A but for 364 puffs of Oregon green experiments.
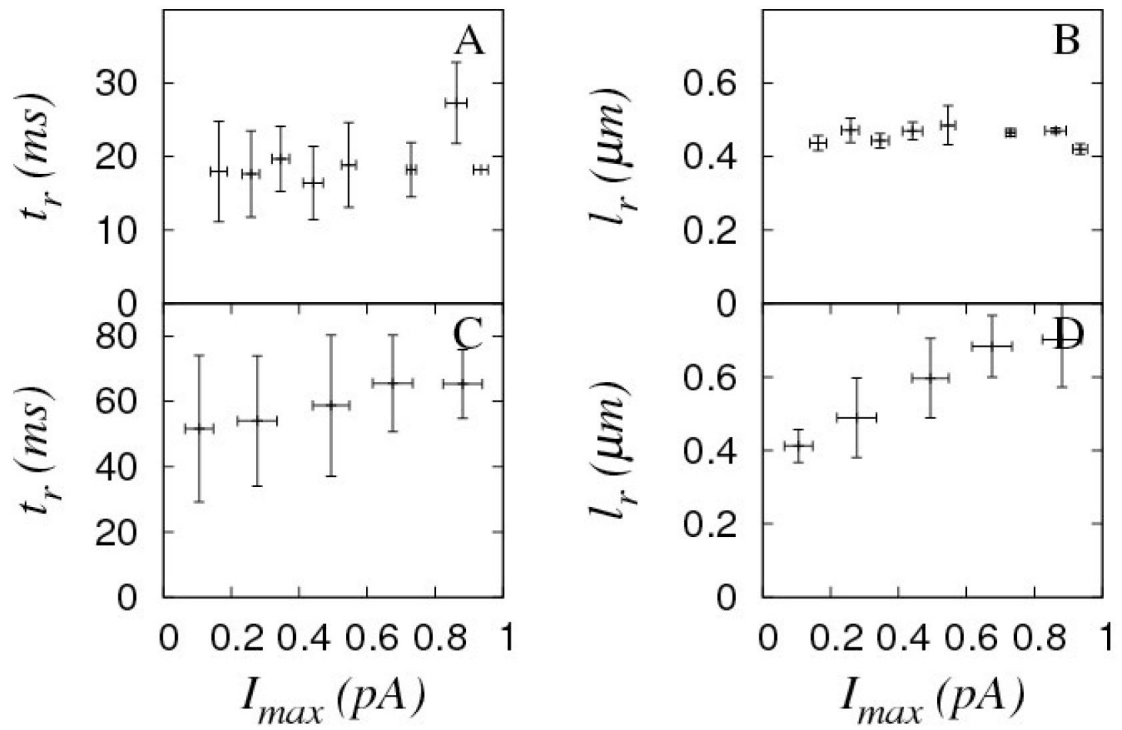
Figure 4.
Dependence of Ca^{2+} flux duration (t_r) and of Ca^{2+} source size (l_r) on the maximum current, I_{max} for Fluo-4 (A,B) and Oregon green (C,D) experiments. Standard deviations and bin sizes of current around mean values are represented with error bars.
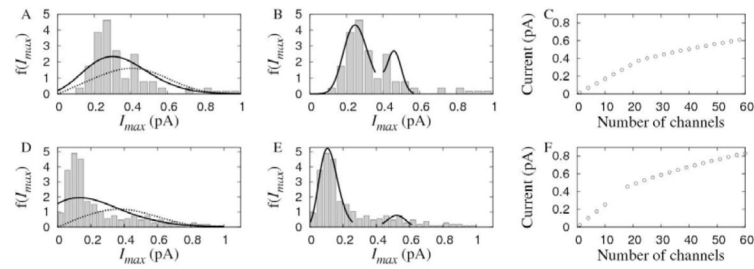
Figure 5.
Current distribution functions for Fluo-4 (A, B) and Oregon green (D,E) experiments. Bars: experimental data. Lines: Theoretical expressions. A: Theoretical expression given by Eq. 15 with $\alpha=1$, $I_o=0.086$pA, $m=4$ (solid line) and with $\alpha=2$, $I_o=0.45$pA and $m=0.72$ (dashed curve). B: Theoretical expression given by Eq. 16-17 with $I_1{}^*=0.36$pA, $I_2{}^*=0.4$pA, $\lambda_1=0.71$, $\alpha_1=1$, $I_{o1}=0.017$pA, $m_1=15$, $\lambda_2=0.27$, $\alpha_2=2$, $I_{o2}=0.08$pA and $m_2=33$. D. Theoretical expression similar to A, but with $\alpha=1$, $I_o=0.19$pA, $m=1.22$ (solid line) and with $\alpha=2$, $I_o=0.56$pA and $m=0.32$ (dashed curve). E: Theoretical expression similar to B but with $\lambda_1=0.71$, $\alpha_1=1$, $I_{o1}=0.025$pA, $m_1=4.72$, $\lambda_2=0.11$, $\alpha_2=2$, $I_{o2}=0.107$pA and $m_2=23.6$. C, F: Current *vs* N_p relationship given by Eq. 14 with $I_{o1}=0.017$pA, $I_{o2}=0.08$pA and $N_{pt}\approx22$ in C and with $I_{o1}=0.025$ pA, $I_{o2}=0.107$pA, in F.
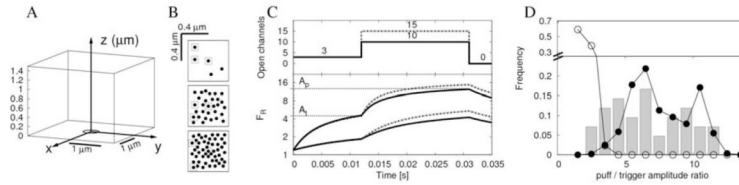
Figure 6.
Simulation of paired trigger-puff events considering 3-channel triggers. A: Geometry of the cytosolic space: a cuboid of dimensions $2.7 \times 2.7 \times 1.5$ μm. The plane z=0 represents the surface of the ER and the circle at the center a cluster of IP$_3$R's. B: Three examples of IP$_3$R distributions within clusters (from top to bottom, N_p=5, 30 and 50). The width of the cluster is constant (0.5 □m). In the figure, the triggering channels are surrounded by boxes. C. Results of the simulation of four paired trigger-puff events. The upper plot shows the number of open channels as a function of time. Three trigger channels open at t=0. At t=0.012s a puff begins with a total of N_p channels simultaneously open. We show results with N_p=10 (solid lines) and N_p=15 (dotted lines). The lower panel shows the corresponding time evolution of the fluorescence signal, F_R. The upper traces correspond to simulations in which the single channel current was I_{ch}=I_o=0.086pA, independent of N_p, while the other two correspond to $N_p I_{ch}$=I, with I given by Eq. 13. We also show the puff and trigger amplitudes obtained in these simulations in the lower panel. D. Comparison of the distributions of puff-to-trigger amplitude ratios obtained from the simulations and from the experiments. The bar plot shows the experimental distribution reported by Rose et al in [2] (the data points were directly captured from their Fig. 4F). The circles correspond to simulations in which the distribution of open channels was assumed to be given by Eq. 11 with m=4 (white circles) or was assumed to be given by the superposition of two Poisson distributions that eventually leads to Eq. 16 (black circles).
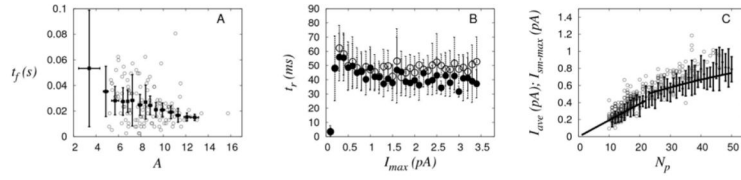
Figure 7. Stochastic puff model
A: Puff duration (t_f) as a function of puff amplitude for experimental observations in *Xenopus laevis* oocytes (open circles) and stochastically simulated puffs obtained using model C_d (black squares and error bars correspond to mean values and standard deviations, respectively). B: Duration of the Ca^{2+} release as a function of the maximum Ca^{2+} current for stochastically simulated puffs obtained using model C_d (black circles) and C_i (open circles). C: Maximum released current (open circles) and averaged current (mean with black dots and standard deviation with vertical lines) released during the events as function of the number of channels in the cluster, N_p, obtained with simulations that use the C_d kinetic model. Superimposed in black, curves that correspond to the $I{\sim}Np$ and $I{\sim}N_p^{1/2}$ scalings for $N_p < 22$ and $N_p > 22$, respectively. In B and C, the maximum released current was obtained from a smoothed version of the simulated $I(t)$.

Table 1

Parameters values used to solve the puff model introduced in Section 2.5 taken from [4].

Parameter	value	Units
Free Calcium:		
D_{Ca}	200	$\mu m^2 s^{-1}$
$[Ca^{2+}]_{basal}$	0.1	μM
Calcium dye (Fluo4-dextran):		
D_{dye}	15	$\mu m^2 s^{-1}$
k_{on-B}	150	$\mu M^{-1} s^{-1}$
k_{off-B}	300	s^{-1}
$[B]_T$	25	μM
Exogenous buffer (EGTA):		
D_{EGTA}	200	$\mu m^2 s^{-1}$
$k_{on-EGTA}$	5	$\mu M^{-1} s^{-1}$
$k_{off-EGTA}$	0.75	s^{-1}
$[EGTA]_T$	40	μM
Endogenous stationary buffer:		
K_{on-S}	400	$\mu M^{-1} s^{-1}$
K_{off-S}	800	s^{-1}
$[S]_T$	40	μM

Table 2

Range of parameters values for the sensitivity analysis.

Parameter	Actual value	Range of variation
D_{Ca}	319 $\mu m^2 s^{-1}$	(80 - 560) $\mu m^2 s^{-1}$
D_{dye}	50 $\mu m^2 s^{-1}$	(12.5 - 250) $\mu m^2 s^{-1}$
k_{on}	100 $\mu M^{-1} s^{-1}$	(10 - 1000) $\mu M^{-1} s^{-1}$